FULLY 3D RAYLEIGH–TAYLOR INSTABILITY IN A BOUSSINESQ FLUID

S. J. WALTERS◉✉[1] and L. K. FORBES◉[1]

Abstract

Rayleigh–Taylor instability occurs when a heavier fluid overlies a lighter fluid, and the two seek to exchange positions under the effect of gravity. We present a linearized theory for arbitrary three-dimensional (3D) initial disturbances that grow in time, and calculate the evolution of the interface for early times. A new spectral method is introduced for the fully 3D nonlinear problem in a Boussinesq fluid, where the interface between the light and heavy fluids is approximated with a smooth but rapid density change in the fluid. The results of large-scale numerical calculation are presented in fully 3D geometry, and compared and contrasted with the early-time linearized theory.

1. Introduction

The accurate modelling of the flow of fluids is an area of ongoing interest and intense research. Such studies have been central in the development of numerous modern technological advances including, but certainly not limited to, heavier-than-air flight, aero-dynamics and hydro-dynamics, aeronautics, supersonic flight and weather prediction. The growth of instabilities is an important area of study, as it leads to an understanding of regions of significant change in the system, such as energy dissipation in the case of vortex formation.

In particular, in this paper we examine the Rayleigh–Taylor instability, which describes the gravitationally unstable situation where a denser fluid sits upon a less dense fluid. Any small disturbance to the initially horizontal interface will grow, allowing the denser fluid to move down and the lighter fluid to rise. This problem was originally described by Lord Rayleigh [13] and further studied by Taylor [17]. Since that time, much work has been carried out investigating the

---

[1]School of Mathematics and Physics, University of Tasmania, P.O. Box 37, Hobart, 7001, Tasmania, Australia; e-mail: stephen.walters@utas.edu.au, larry.forbes@utas.edu.au.

behaviour, largely of the two-dimensional case. Increasingly, however, modelling of fully three-dimensional (3D) systems is becoming possible with the ongoing increases in computing performance. The review by Sharp [16] gives a summary of some of the work undertaken in this large field of research. More recently, reviews by Abarzhi [1] and Zhou [19, 20] particularly considered the energy dissipation aspect and the self-similar nature of Rayleigh–Taylor mixing, and hence the transition to turbulent flow. Apart from finite-difference, finite-element and spectral methods, modern approaches to the numerical simulation of the Rayleigh–Taylor instability include the use of the Cahn–Hilliard equation with various numerical schemes [9], the lattice Boltzmann method [10] and smoothed particle hydrodynamics methods [15], to mention only a few of the large number of approaches to this problem.

The purpose of this paper is to study 3D Rayleigh–Taylor flow, and determine to what extent linearization might retain some predictive power at early times, and to explore some fully 3D outflow morphologies, from simple initial disturbances. To do this we will use the Boussinesq approximation (see the article by Farrow and Hocking [6]), which is a valid approach if the densities of the two fluids are similar. The velocity–vorticity formulation will obviate the need to solve for the pressure explicitly, which is computationally expensive to do accurately. A bi-streamfunction approach will avoid the need to solve the incompressibility equation (Laplace's equation for the velocity potential) at each time step, so eliminating another expensive computational task. These streamfunctions and the density perturbation will be represented as Fourier series, which means that derivatives can be evaluated explicitly in terms of the basis functions. Such spectral methods exhibit exponential convergence [4, pages 45–46], and are eminently suitable for solutions which are smooth and in simple geometries, both of which apply to the problem studied in this paper. Finally, the resultant large set of independent calculations will be solved on a graphical processing unit (GPU) which is designed to handle many simple calculations in parallel. We will demonstrate that this combination of approaches leads to a highly accurate modelling of fully 3D fluid flow problems using enough precision to show clearly the features of the flow.

2. Theoretical framework

The equations describing the Rayleigh–Taylor problem for incompressible fluids are the equation for conservation of mass (incompressibility condition), equation (2.1), and the incompressible Navier–Stokes equation (2.2):

$$\boldsymbol{\nabla} \cdot \boldsymbol{q} = 0, \tag{2.1}$$

$$\frac{\partial \boldsymbol{q}}{\partial t} + (\boldsymbol{q} \cdot \boldsymbol{\nabla})\boldsymbol{q} - \frac{\mu}{\rho}\nabla^2 \boldsymbol{q} = \boldsymbol{g} - \frac{\boldsymbol{\nabla} p}{\rho}. \tag{2.2}$$

Here, $\boldsymbol{q}$ is the velocity field, μ is the dynamic viscosity, ρ is the density, p is the pressure and $\boldsymbol{g}$ is the acceleration due to gravity.

Whether using primitive variables or spectral or other methods, these equations are computationally expensive to solve numerically, usually requiring the forward integration of a large system of differential equations.

In the current paper, we use a 3D spectral method similar to that used by Forbes [7] who solved the viscous Rayleigh–Taylor problem in two dimensions using a Boussinesq approximation.

In recent years, computational speeds have continued to increase, and this paper re-examines the problem with more powerful computer hardware. We have been able to extend Forbes' original work into a fully 3D problem. A decrease in required computing time of more than two orders of magnitude has been achieved with newer hardware and parallelization. This has allowed us to compute the evolution of the interface in three dimensions with sufficient accuracy and precision to observe in detail the expected roll-over of the interface. In addition, as the problem can now be made fully 3D, we will present images of flow resulting from initial conditions which are neither spherically nor axially symmetric.

3. Linearized inviscid model

We first consider the simpler case where we assume that there is no viscosity in the two fluids. This will give a solution to the Rayleigh–Taylor instability which will be valid for early times. Such a solution provides a means of validating the numerical solution, at least for early times, and gives confidence that the numerical scheme is suitable. The following linearization is similar to that of Taylor [17], but is slightly more general in that it includes the effects due to finite depth, contains a 3D analysis, rather than two-dimensional (2D), and also discusses the difference in behaviour due to different modes in the initial disturbance.

In this inviscid case, if the two layers of fluid are initially at rest, and the interface between them is a small perturbation to a known function, a linearized system can be constructed which is valid for early times. In the 3D Rayleigh–Taylor model, we assume that the interface is a horizontal plane with a small perturbation function.

The problem is constructed such that the denser fluid layer "fluid 2" sits upon the lighter layer of "fluid 1". We specify that the "floor" is at $z = -H_1$ and the "ceiling" is at $z = H_2$. The initial interface between the fluids is situated at $z = 0$. The assumption that the fluids are inviscid means that the flow is irrotational, $\nabla \times \boldsymbol{q} = 0$. This condition is met through the use of a velocity potential for each fluid, so that in each fluid the velocity field $\boldsymbol{q}$ takes the form $\boldsymbol{q} = \nabla \Phi$ for a potential field Φ. This allows integration of the equations of motion for each fluid ($j = 1, 2$) to give the Bernoulli equations [3, page 83].

$$\frac{\partial \Phi_j}{\partial t} + \frac{1}{2}(u_j^2 + v_j^2 + w_j^2) + \frac{p_j}{\rho_j} + gz = 0, \quad j = 1, 2. \tag{3.1}$$

In addition, since the flow is irrotational in this inviscid case, the substitution of $\boldsymbol{q} = \nabla \Phi$ into the conservation of mass equations (2.1) results in Laplace's equation in

each fluid:

$$\nabla^2 \Phi_j = 0, \quad j = 1, 2.$$

The functions Φ_1 and Φ_2 are, respectively, the velocity potentials in the two fluids.

We consider an interface between the two fluids at $z = \eta(x, y, t)$. The pressures immediately to either side of the interface must be equal, so that at $z = \eta$, $p_1 = p_2$. Rearranging equation (3.1) for pressure, this equality at the interface gives the dynamic constraint

$$\rho_1 \left[\frac{\partial \Phi_1}{\partial t} + \frac{1}{2}(u_1^2 + v_1^2 + w_1^2) + gz \right] = \rho_2 \left[\frac{\partial \Phi_2}{\partial t} + \frac{1}{2}(u_2^2 + v_2^2 + w_2^2) + gz \right] \quad (3.2)$$

on $z = \eta$.

We now introduce dimensionless variables, by scaling with the gravitational constant g and the size of the computational window L. The conversion to these variables is

$$(\hat{x}, \hat{y}, \hat{z}, \hat{H}_1, \hat{H}_2, \hat{\eta}) = \frac{2\pi}{L}(x, y, z, H_1, H_2, \eta),$$

$$\hat{t} = \sqrt{\frac{2\pi g}{L}} t,$$

$$\hat{q} = \sqrt{\frac{2\pi}{gL}} q,$$

$$\hat{\Phi} = \sqrt{\frac{8\pi^3}{gL^3}} \Phi.$$

We will use these new variables, but drop the hats for readability. In these variables, and introducing $D = \rho_2/\rho_1$ as the dimensionless ratio of densities, equation (3.2) becomes

$$\frac{\partial \Phi_1}{\partial t} + \frac{1}{2}(u_1^2 + v_1^2 + w_1^2) + z = D \left[\frac{\partial \Phi_2}{\partial t} + \frac{1}{2}(u_2^2 + v_2^2 + w_2^2) + z \right] \quad \text{on } z = \eta.$$

In the state where the interface is perfectly flat at $z = 0$, and where both fluids are at rest, equation (3.2) is satisfied, as all the terms in the brackets are zero. We will expand about this zero-state (unstable) equilibrium using a small dimensionless parameter ϵ for the shape of the interface and the velocity potentials:

$$\eta(x, y, t) \equiv 0 + \epsilon \eta^L(x, y, t) + O(\epsilon^2),$$

$$\Phi_1(x, y, z, t) \equiv 0 + \epsilon \Phi_1^L(x, y, z, t) + O(\epsilon^2),$$

$$\Phi_2(x, y, z, t) \equiv 0 + \epsilon \Phi_2^L(x, y, z, t) + O(\epsilon^2),$$

where the superscript L denotes the linearized variable.

The linearized problem then takes the form of Laplace's equation for each fluid:

$$\nabla^2 \Phi_2^L = 0 \quad \text{in } 0 < z < H_2,$$

$$\nabla^2 \Phi_1^L = 0 \quad \text{in } -H_1 < z < 0, \quad (3.3)$$

where the kinematic boundary conditions are

$$\frac{\partial \Phi_1^L}{\partial z} = 0 \quad \text{on } z = -H_1,$$

$$\frac{\partial \Phi_2^L}{\partial z} = 0 \quad \text{on } z = H_2,$$

$$\frac{\partial \Phi_1^L}{\partial z} = \frac{\partial \eta^L}{\partial t} \quad \text{on } z = 0, \tag{3.4}$$

$$\frac{\partial \Phi_2^L}{\partial z} = \frac{\partial \eta^L}{\partial t} \quad \text{on } z = 0.$$

The dynamic boundary condition, equation (3.2), linearizes to

$$(D - 1)\eta^L + D\frac{\partial \Phi_2^L}{\partial t} - \frac{\partial \Phi_1^L}{\partial t} = 0 \quad \text{on } z = 0. \tag{3.5}$$

We begin formulating a solution to Laplace's equation (3.3) in each fluid separately. Using standard separation of variables techniques, for an (m, n)th Fourier mode, we may write

$$\Phi_1^L(x, y, z, t) = A_1(t) \cos(mx) \cos(ny) \cosh(\xi(z + H_1)), \tag{3.6}$$
$$\Phi_2^L(x, y, z, t) = A_2(t) \cos(mx) \cos(ny) \cosh(\xi(H_2 - z)),$$

where we have written $\xi \equiv \sqrt{m^2 + n^2}$ for convenience. Since the problem is linear, we may later superpose these models for a more general shape of the initial interface.

We now need to solve for $A_1(t)$ and $A_2(t)$. Describing the (m, n)th mode of the interface as $\eta^L(x, y, t) = G(t) \cos(mx) \cos(ny)$, and substituting into equation (3.4), as well as equation (3.6),

$$\frac{dG(t)}{dt} = A_1(t)\xi \sinh(\xi H_1). \tag{3.7}$$

Then equation (3.5), which is the dynamic condition at $z = 0$, may be written as

$$(D - 1)G(t) + D\frac{dA_2}{dt} \cosh(\xi H_2) - \frac{dA_1}{dt} \cosh(\xi H_1) = 0.$$

With equation (3.7), this yields a second-order linear equation for $G(t)$, which may be solved to yield

$$G(t) = C_1 e^{\alpha t} + C_2 e^{-\alpha t},$$

where the constant α is given by

$$\alpha = \sqrt{\frac{(D - 1)\xi}{D \coth(\xi H_2) + \coth(\xi H_1)}}. \tag{3.8}$$

This parameter α depends on the integers m, n and gives the growth rate for the (m, n)th mode. The constants C_1 and C_2 are determined by the initial conditions. If, for

example, the interface starts from rest, then $G'(t) = 0$ at $t = 0$, so that $C_1 = C_2$ and then $G(t) = C_{mn} \cosh(\alpha t)$ for an interface disturbance at the (m, n)th mode. Thus, the linearized behaviour of any interface may be written as the sum of contributions from each mode:

$$\eta(x, y, t) = \epsilon \sum_{m=0}^{\infty} \sum_{n=0}^{\infty} C_{mn} \cosh(\alpha t) \cos(mx) \cos(ny) + O(\epsilon^2). \tag{3.9}$$

The C_{mn} coefficients are determined from the initial shape of the interface. So, the linearized solution predicts that any small disturbance to the initially flat interface will grow exponentially, with growth rates given by (3.8). The highest modes have largest m, n and therefore largest α, and so they will dominate. That is, the linearized solution at time t will be a superposition of the initial modes multiplied by exponential factors. As expected, this solution cannot "roll over", but does give an accurate description of the behaviour of the interface for early times. We will compare this with the numerical solution to the nonlinear viscous problem in Section 6.

4. Boussinesq viscous model

We now include viscosity in the system, using a Boussinesq approximation. As in Section 3, we are considering a system with a denser fluid sitting on top of a lighter fluid. However, in the Boussinesq model [6], we approximate this by a single fluid with a density which changes rapidly but smoothly across the region where the sharp interface would be in the two-fluid model. This difference in density will drive the motion as it did in the linear model of Section 3. In this nonlinear model, however, we note that the density difference will slowly be reduced by diffusion over time.

Returning briefly to dimensional variables, let the original two fluids have densities ρ_1 and ρ_2. Then we define the single density for the Boussinesq fluid as a constant (the original density of fluid 1) and a small perturbation to that density, which varies over time and space: $\rho(x, y, z, t) = \rho_1 + \tilde{\rho}(x, y, z, t)$. The equations governing this system are now, respectively, the incompressibility condition, the transport equation for the density perturbation and the incompressible Navier–Stokes–Boussinesq equation:

$$\boldsymbol{\nabla} \cdot \boldsymbol{q} = 0,$$

$$\frac{\partial \tilde{\rho}}{\partial t} + (\boldsymbol{q} \cdot \boldsymbol{\nabla})\tilde{\rho} = \sigma \nabla^2 \tilde{\rho},$$

$$\frac{\partial \boldsymbol{q}}{\partial t} + (\boldsymbol{q} \cdot \boldsymbol{\nabla})\boldsymbol{q} + \frac{1}{\rho_1}\boldsymbol{\nabla} p = \frac{1}{\rho_1}[-(\rho_1 + \tilde{\rho})g\boldsymbol{k} + \mu \nabla^2 \boldsymbol{q}]. \tag{4.1}$$

Here, μ is the dynamic viscosity, $\boldsymbol{k}$ is the unit vector in the z-direction and σ is the diffusion coefficient for density. It is related to a Prandtl number, as discussed by Farrow and Hocking [6]. In order to avoid calculating the pressure in this last equation, which is computationally expensive, and not necessary for determining the flow, we will solve the vorticity equation instead. By taking the curl of equation (4.1), we remove the pressure term from the equation. Defining the vorticity vector field

as $\boldsymbol{\zeta} \equiv \{\zeta^X, \zeta^Y, \zeta^Z\} = \boldsymbol{\nabla} \times \boldsymbol{q}$, the curl of the momentum equation gives the vorticity equation [3, page 267]:

$$\frac{\partial \boldsymbol{\zeta}}{\partial t} + (\boldsymbol{q} \cdot \boldsymbol{\nabla})\boldsymbol{\zeta} - (\boldsymbol{\zeta} \cdot \boldsymbol{\nabla})\boldsymbol{q} = -\frac{g}{\rho_1}\boldsymbol{\nabla} \times (\tilde{\rho}\boldsymbol{k}) + \mu\nabla^2\boldsymbol{\zeta}. \tag{4.2}$$

As with the linearized inviscid problem, we now switch to dimensionless variables using the same conversion constants g, L and ρ_1. The conversion for the two additional variables is

$$\hat{\tilde{\rho}} = \frac{\tilde{\rho}}{\rho_1},$$

$$\hat{\boldsymbol{\zeta}} = \sqrt{\frac{L}{2\pi g}}\boldsymbol{\zeta}.$$

In dimensionless variables, equations (4.1) and (4.2) then become

$$\hat{\boldsymbol{\nabla}} \cdot \hat{\boldsymbol{q}} = 0,$$

$$\frac{\partial \hat{\tilde{\rho}}}{\partial t} + (\hat{\boldsymbol{q}} \cdot \hat{\boldsymbol{\nabla}})\hat{\tilde{\rho}} = \hat{\sigma}\hat{\nabla}^2\hat{\tilde{\rho}}, \tag{4.3}$$

$$\frac{\partial \hat{\boldsymbol{\zeta}}}{\partial \hat{t}} + (\hat{\boldsymbol{q}} \cdot \hat{\boldsymbol{\nabla}})\hat{\boldsymbol{\zeta}} - (\hat{\boldsymbol{\zeta}} \cdot \hat{\boldsymbol{\nabla}})\hat{\boldsymbol{q}} = -\hat{\boldsymbol{\nabla}} \times (\hat{\tilde{\rho}}\boldsymbol{k}) + \hat{\mu}\hat{\nabla}^2\hat{\boldsymbol{\zeta}}, \tag{4.4}$$

where $\hat{\mu} = \mu(2\pi/L)^{3/2}g^{-1/2}\rho_1^{-1}$. Notice that here the dimensionless viscosity $\hat{\mu}$ is the inverse of a Reynolds number. As in Section 3, we will use these dimensionless variables, but for readability we will omit the hats.

In order to confine our computations to a finite region, we stipulate that fluid may not cross the boundary of the computational window. Thus, we require the following conditions on the velocity components:

$$\begin{aligned}
u &= 0 & &\text{at } x = \pm\pi, \\
v &= 0 & &\text{at } y = \pm\pi, \\
w &= 0 & &\text{at } z = -H_1, H_2.
\end{aligned} \tag{4.5}$$

The incompressibility condition and these boundary conditions are met using a certain spectral representation. The incompressibility condition is satisfied identically by choosing to let the velocity field $\boldsymbol{q}$ be the curl of some vector field $\boldsymbol{V} \equiv \{V_1, V_2, V_3\}$. Only two independent components are required, so we are free to choose one of these components. Following the approach of Forbes and Brideson [8], we let $V_3 = 0$ and rename $V_1 \equiv \Psi$ and $V_2 \equiv \chi$. Using lower case coordinate subscripts to denote partial derivatives, the velocity components are

$$\begin{aligned}
u &= -\chi_z, \\
v &= \Psi_z, \\
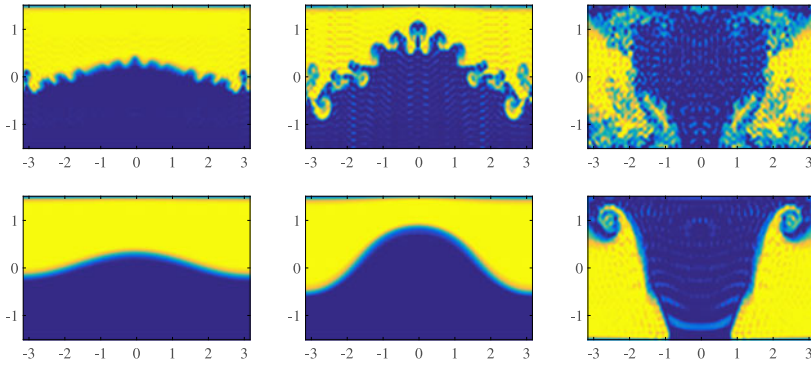w &= \chi_x - \Psi_y,
\end{aligned}$$

FIGURE 1. A 2D slice of the 3D interface is shown at dimensionless times $t = 21$ (left), $t = 28$ (centre) and $t = 42$ (right) for calculations performed using single precision (upper) and double precision (lower). The use of single-precision values in the upper images has produced multiple numerical artefacts which obscure the solution more and more as time passes. The use of double-precision values removed these artefacts as seen in the lower three images (colour available online).

and the incompressibility condition

$$u_x + v_y + w_z = 0$$

is met identically. In order to meet the boundary conditions (4.5), we use a spectral representation of Ψ, χ as

$$\chi(x, y, z, t) = \sum_{m=0}^{\infty} \sum_{n=0}^{\infty} \sum_{p=1}^{\infty} A_{mnp}(t) \sin(\alpha_m x) \cos(\alpha_n y) \sin(\alpha_p(z + H_1)),$$

$$\Psi(x, y, z, t) = \sum_{m=0}^{\infty} \sum_{n=0}^{\infty} \sum_{p=1}^{\infty} B_{mnp}(t) \cos(\alpha_m x) \sin(\alpha_n y) \sin(\alpha_p(z + H_1)), \qquad (4.6)$$

with the coefficients $\alpha_m, \alpha_n, \alpha_p$ chosen to meet the boundary conditions, and the integers m, n, p being the spectral modes. We initially chose basis functions with $\alpha_m = m, \alpha_n = n, \alpha_p = p\pi/(H_1 + H_2)$. This means that the particular solution in this case will be left–right symmetric in x and y, but need not be symmetric in z. If we wish to examine solutions which are not necessarily symmetric about the x and y axes, we can choose basis functions as we have for z. We will also use a spectral representation for the density term $\tilde{\rho}$:

$$\tilde{\rho}(x, y, z, t) = \sum_{m=0}^{\infty} \sum_{n=0}^{\infty} \sum_{p=1}^{\infty} C_{mnp}(t) \cos(\alpha_m x) \cos(\alpha_n y) \sin(\alpha_p(z + H_1)). \qquad (4.7)$$

With the choice of sine for the z basis functions, this forces the fluid to have zero density perturbation on the top and bottom boundaries at all times, as can be seen in Figure 1. To correct this restriction, simulations were then run with $\alpha_p = p\pi/\{(H_1 + H_2)/2\}$, which allows the density to take any value throughout
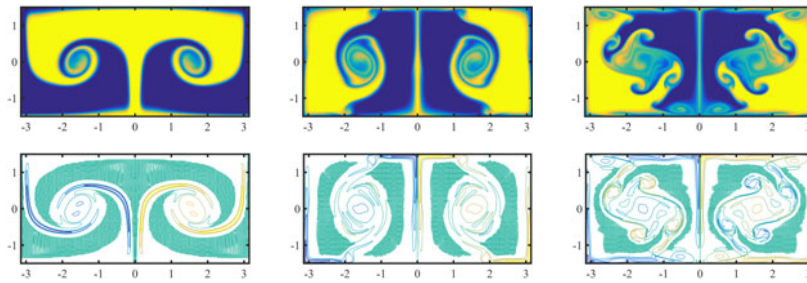
FIGURE 2. 2D interface, with initial interface perturbation shown at times $t = 45$ (left-hand column), $t = 54$ (middle column) and $t = 63$ (right-hand column). The less dense fluid is shown in a lighter shade (yellow online) and the denser fluid in a darker shade (blue online). These calculations used 1280 points and 382 modes in the x-direction and 640 points and 191 modes in y. The two axes have equal scales. The upper row shows the density, while the lower row shows the vorticity.
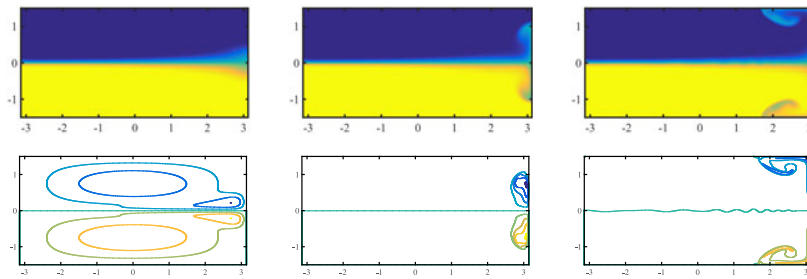

FIGURE 3. 2D interface, with initially rotational flow, shown at times $t = 45$ (left-hand column), $t = 60$ (middle column) and $t = 75$ (right-hand column). The upper row shows the density perturbation. The less dense fluid is shown in a lighter shade (yellow online) and the denser fluid in a darker shade (blue online). The lower row shows the corresponding vorticity. These calculations used 1600 points and 400 modes in the x-direction and 800 points and 200 modes in y. The two axes have equal scales.

the fluid. This change may be seen in Figures 2 and 3, where there are no thin layers of fluid at top or bottom of the region. We substitute these representations into the equations for vorticity (4.4) and transport (4.3), and solve for the sets of derivatives of coefficients A_{mnp}, B_{mnp} and C_{mnp}. Each coefficient can be isolated by multiplication by the appropriate basis functions and integrating over the computational space, using the orthogonality of the trigonometric functions. The final system of equations to be solved numerically is too lengthy to include here, but is described in Appendix A.

5. Notes on computing system and performance

The 3D computations reported in this paper were performed using an Intel I7-7700 CPU with 32 GB RAM and a Quadro GP100 GPU running Ubuntu 17.10. The computations were written in Fortran and compiled using the PGI Fortran compiler [12], with ACC directives moving most of the calculations to the GPU.

The output from the program was an array of data for $\tilde{\rho}$ at each chosen time. This data was read into MATLAB to produce the figures.

In the process of testing our novel spectral techniques, it was discovered that numerous unexpected artefacts became apparent in the 3D models. This was determined to be due to the use of single-precision calculations, for which many graphics cards are optimized. This problem was resolved by using a GPU designed for fast double-precision calculations. In Figure 1, we show the difference between single-precision and double-precision calculations in an otherwise identical numerical routine. The top three panels illustrate the growth of a single-mode Rayleigh–Taylor instability with density ratio $D = 1.05$, from initial amplitude $\epsilon = 0.03$ at the three times $t = 21, 28, 42$, computed at single precision. The lower three panels are for the identical conditions, except that here the results were generated using double-precision arithmetic.

Both sets of results were taken from the centre plane $y = 0$ of a fully 3D calculation. Clearly the single-precision results in the upper three frames have suffered the growth of inaccuracies due to the use of 32-bit floats in the computations and the resultant accumulation of round-off errors. This is equivalent to adding small disturbances in very high modes. Once these higher modes are formed, they then grow as Rayleigh–Taylor instabilities in their own right. As shown in the linearized analysis, higher modes grow faster than lower modes, at least initially.

No such problems occur with the more accurate double-precision results shown in the lower three diagrams at the same three times, where now the interfacial roll-up at the last time $t = 42$ is clearly visible. Although computer run times were increased by a factor of two to three times, it was nevertheless found to be necessary to run all 3D programs using double-precision arithmetic, due to the extremely large number of computations needed in fully 3D computations.

6. Results

6.1. Two-dimensional calculations   Repeating the earlier 2D model of Forbes [7] with the approach described in Section 5 resulted in a decrease in computational time by a factor of approximately 250. This allowed the use of a much greater number of mesh points and spectral modes which improved accuracy, allowing the integration to continue far past the "roll-over" point. The results are also able to be observed with much higher resolution. In Figure 2, we present the rolled-up 2D interface at dimensionless times $t = 45$, $t = 54$ and $t = 63$. The surface started from an initial interface shape $y = \epsilon \cos x$, with $\epsilon = 0.03$. Specifically, the initial density perturbation is set at $\tilde{\rho} = 0.05/[1 + \exp(100\{0.03 \cos(x) - y\})]$. This gives an interfacial region in which the density perturbation changes smoothly, but very rapidly, from $\tilde{\rho} = 0$ to $\tilde{\rho} = 0.05$. The system of spectral coefficients described in Section 4 in equations (4.6) and (4.7), and detailed in Appendix A (but limited to two dimensions), were incorporated into the transport and momentum equations (4.1), and were integrated forward in time using the classical fourth-order Runge–Kutta method given by

Atkinson [2, page 371]. This can be adapted easily for 2D and 3D systems of ordinary differential equations, which allows parallelization of the computation. The less dense fluid (yellow online) initially has dimensionless density parameter 1, and the denser fluid (blue online) has density ratio $D = 1.05$. The computational window extends from $-\pi$ to π in the x-direction, and from -1.5 to 1.5 in the z-direction. This last constraint causes the typical mushroom shape to flatten out as it approaches the ceiling. If a less constrained flow is desired, the computational "walls" can be moved further away, or the initial perturbation can be reduced in width (the latter approach was taken in the 3D case in Section 6.2). We see that as the lighter fluid rises through the denser fluid, it entrains the denser fluid, causing it both to roll up and over and then to rise again in two central plumes. The run time for this computation at 1280 by 640 grid points, and 382 by 191 spectral modes, was 14 h. Past the times shown, the fluids continue to swirl around, and gradually their densities equalize through diffusion. These Kelvin–Helmholtz-type roll-up effects are characteristic of Rayleigh–Taylor instabilities where the density ratio is small. Daly [5] described the variation in this effect at density ratios of 1.1, 2 and 10. While spiral formation is found at $D = 1.1$, none is seen in the high-density-difference $D = 10$ case. The Boussinesq approximation adopted in this paper assumes that the density ratio is close to 1, and we set $D = 1.05$ in all simulations.

A different 2D example is shown in Figure 3, with the initial condition being an initial velocity field rather than an interfacial perturbation. Counter-rotating flows have been established at time $t = 0$ in the two fluids, which now have a horizontal interface at $y = 0$. As may be seen in the left-hand frame at $t = 45$, a mixing region develops, which is pushed around the outside of the region by the initial flow. In the right-hand frame ($t = 75$), it may be seen that an instability is growing on the interface at $y = 0$. This instability develops at varying times depending on the number of grid points and modes, and is therefore thought to be initiated by round-off error. Once initiated, these disturbances then grow as any Rayleigh–Taylor-type disturbance must. This simulation was performed with 1600 by 800 grid points and 400 by 200 modes, and took 32 h to run.

6.2. Three-dimensional calculations   A similar procedure was used for generating and displaying the results of the 3D model. As for the 2D system, the sets of spectral coefficients A_{mnp}, B_{mnp} and C_{mnp} were integrated forward in time using the classical fourth-order Runge–Kutta method. At any time, the density $\tilde{\rho}$ can be reconstructed from the coefficients C_{mnp}. We begin with an interface with initial shape, symmetric in x and y,

$$z_0 = \frac{\epsilon}{4}\{1 + \cos(2x)\}\{1 + \cos(2y)\}, \quad -\pi/2 < x < \pi/2, \quad -\pi/2 < y < \pi/2,$$

$$z_0 = 0, \quad \text{elsewhere.}$$

Similar to the 2D case shown in Figure 2, the initial interface is approximated by setting $\tilde{\rho} = 0.05/[1 + \exp(100(z_0 - z))]$. The system is allowed to evolve with $\tilde{\rho}$ reconstructed and plotted at intervals. In order to clarify the display of the interface in three dimensions, only the interfacial points are displayed, rather than colouring
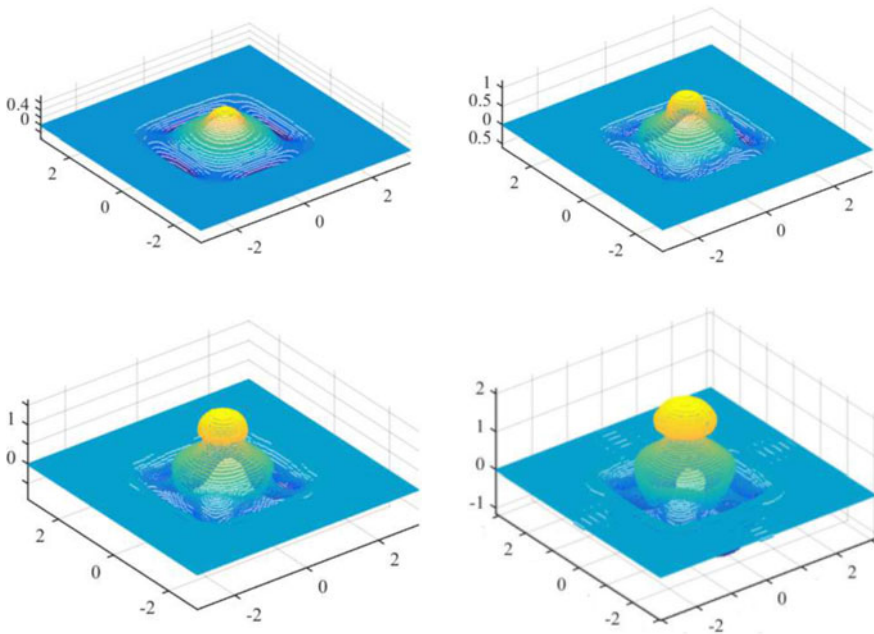
FIGURE 4. 3D interface at $t = 20$ (upper left), $t = 22.5$ (upper right), $t = 25$ (lower left) and $t = 27.5$ (lower right). The shading (colour online) indicates the z-value of the interface at that point. These calculations used 192 points in each direction and 36 modes in each variable.

each point in the computational region according to its density value, as was done for the 2D model. These interfacial points are defined to be the points where the density perturbation changes from less than $(D - 1)/2$ to more than $(D - 1)/2$. In Figure 4, we present results for $\epsilon = 0.03$, $H_1 = 1.5$ and $H_2 = 8$. The viscosity and diffusion parameters were set to $\mu = 10^{-4}$ and $\sigma = 10^{-4}$. The regular grid of points consisted of 192 points in each of the x-, y- and z-directions, and 36 Fourier modes for each of m, n and p. We have shown the interface at dimensionless times 20, 22.5, 25 and 27.5. The upward movement of the lighter plume, and the downward movement of the surrounding denser fluid, are readily apparent at these times. The plume forms the expected bulbous top which rolls over as it rises. Note that the final frame shows Gibbs' phenomenon [18] due to the formation of a very steep density gradient near $x, y = \pm\pi/2$. This can be reduced by the use of a greater number of Fourier modes.

As this model has been developed in fully 3D coordinates, we are free to give a 3D initial condition, rather than one in which the x components are the same as the y components, as in Figure 4. We thus start with an interface as follows:

$$z = \frac{\epsilon}{4}(1 + \cos(4x/3))(1 + \cos(4y)), \quad -3\pi/4 < x < 3\pi/4, \quad -\pi/4 < y < \pi/4,$$
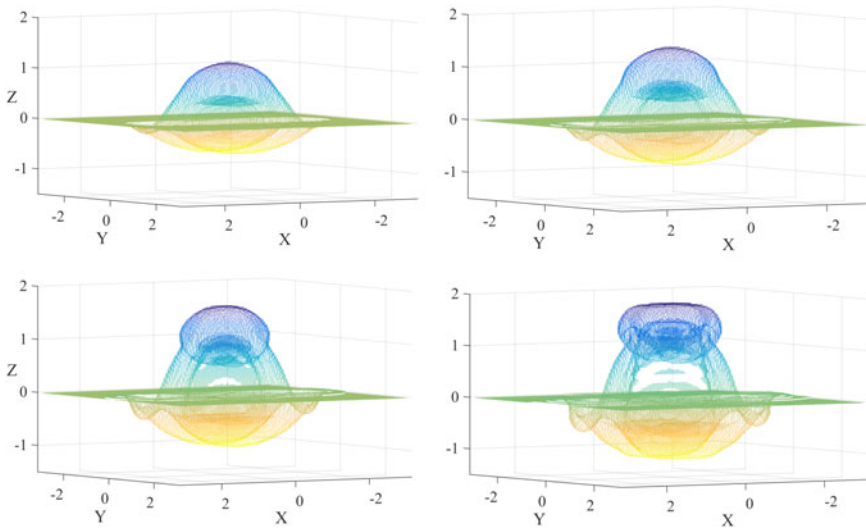
$$z = 0, \quad \text{elsewhere.}$$

FIGURE 5. 3D interface at $t = 22$ (upper left), $t = 24$ (upper right), $t = 26$ (lower left) and $t = 28$ (lower right). As in Figure 4, the colour indicates the z-value of the interface at that point, but reversed to enhance visualization of the interface. The interface begins as a small lump, longer in the x-direction than in the y-direction, before dividing into a structure with two separated "legs". The flattening effect of a low ceiling at $z = 2$ is apparent in the final frame (lower right).

Figure 5 shows the evolution of this interface for parameters $\epsilon = 0.03$, $H_1 = 1.5$, $H_2 = 2$, $\mu = 10^{-3}$ and $\sigma = 10^{-4}$. This calculation was performed using 128 points and 32 modes in each direction. Note that the interface initially grows exponentially, as expected from the inviscid linear analysis in Section 3. However, the middle section of the interface then splits into a shape with two "legs" connecting the overturning top to the lower part of the interface. In the last frame we see the effect of the low ceiling height in flattening the top of the overturning structure. This calculation took approximately 7 h.

The initial disturbance shape used to produce Figure 5 was again used, but with the Reynolds number decreased by a factor of 10, in order to show the effects of greater viscosity. We have also increased the ceiling height to allow the simulation to run for longer, without being flattened by interaction with the ceiling. The very different results are shown in Figure 6. The much greater viscosity slows the rising of the plume, allowing the formation of a "mushroom" cap. Towards the end of the run, the stem of the plume is starting to bunch into knots and is shedding rings of fluid near the base. As in Figure 4, we set $H_1 = 1.5$, $H_2 = 8$ and $\sigma = 10^{-4}$, but $\mu = 10^{-2}$. With 160 grid points and 32 modes in each direction, this simulation took 12 h.

A very different flow involves an initially spherical drop of fluid rising or falling through a surrounding fluid of slightly different density. In Figure 7, buoyancy is causing a slightly less dense fluid, initially at rest, to rise through the denser
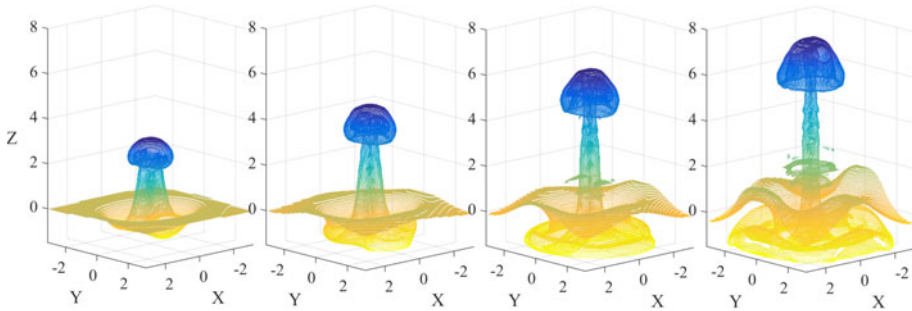
FIGURE 6. 3D interface for viscous plume at (from left to right): $t = 42$, $t = 49.2$, $t = 56.4$ and $t = 63.6$. The colour indicates the z-value of the interface at that point. These calculations used 160 grid points and 32 spectral modes in the x-, y- and z-directions. The axes have equal scales.
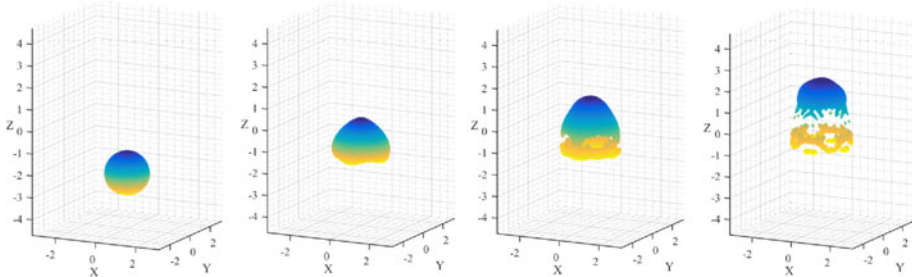

FIGURE 7. 3D rising bubble at (from left to right): $t = 5$, $t = 20$, $t = 30$ and $t = 40$. The colour indicates the z-value of the interface at that point. These calculations used 200 grid points and 40 spectral modes in the x- and y-directions and 300 points and 60 modes in the z-direction. The axes have equal scales.

surrounding fluid. The initially symmetric sphere (frame 1) can be seen to be distorted by the effect of the walls on the flow of the heavier fluid past the sphere of less dense fluid (frame 2). In the third frame we see that this denser fluid flowing down has caused a ring of material to slow and detach from the bottom of the sphere, leaving a faster rising cap. This simulation was in a box ($-\pi < x < \pi$, $-\pi < y < \pi$, $-3\pi/2 < z < 3\pi/2$), with an initial sphere of low-density fluid of radius 1, centred on the z-axis at $z = -0.75\pi$. In this case, the density perturbation was simply set as 0 inside the sphere and 0.05 outside. In order to reduce Gibbs' phenomenon due to this sharp interface, the initial C_{mnp} coefficients for the density were smoothed using a Lanczos smoothing parameter of 0.05. The run time for this calculation using 200 grid points and 40 spectral modes in the x- and y-directions and 300 points and 60 modes in the z-direction was 50 h.

A non-Rayleigh–Taylor flow (that is, one with no gravitational effects) is shown in Figure 8, which shows two toroidal blobs of fluid colliding. This simulation
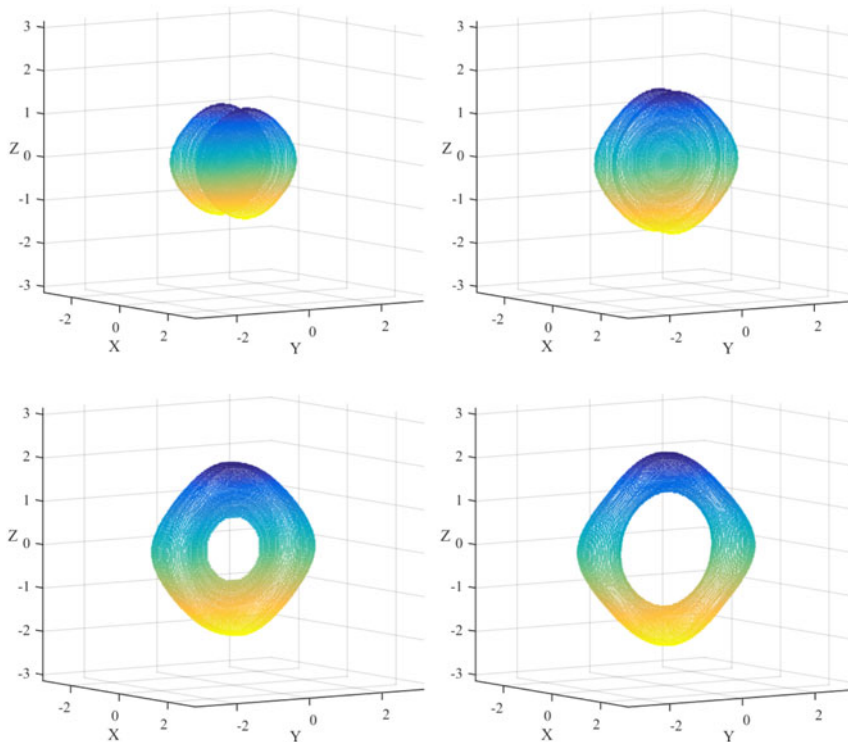
FIGURE 8. Colliding toroidal blobs at four dimensionless times, $t = 120, 240, 360, 480$, from top left to bottom right. The boundaries are at $\pm\pi$ in each direction. An initial velocity field moves the blobs together until they collide, flatten and spread.

was inspired by an experimental work [11] and the fascinating recreation of that experiment [14]. We start with two toroidal blobs of neutral buoyancy ($\tilde{\rho} = 0$), with an initial velocity towards the $x = 0$ plane. The neutral buoyancy condition is met by setting the gravitational force to zero; $\tilde{\rho}$ is now just a marker for the different fluid, and may be considered to represent the colour, opacity or some other characteristic of the fluid, which differentiates it from the surrounding medium. The blobs collide and flatten to form a single structure, thinning in x and spreading in y and z. The blobs of fluid have an initial surface given by $r^2 = (x \pm 1)^2 + (0.5 - \sqrt{0.9y^2 + z^2})^2$, and an initial velocity field set by $\chi = \pm y/200$ and $\Psi = \pm z/200$ moving the fluid blobs towards the $x = 0$ plane. The computational region is bounded by $\pm\pi$ in each direction, with $\sigma = 10^{-4}$, $\mu = 10^{-3}$. Using 160 points and 40 modes in each direction, this simulation took 47 h to run. Note that while the fine details seen in the experimental works [11, 14] are not able to be reproduced at the resolution used here, this simple simulation is included to demonstrate the versatility of the approach presented in this paper.
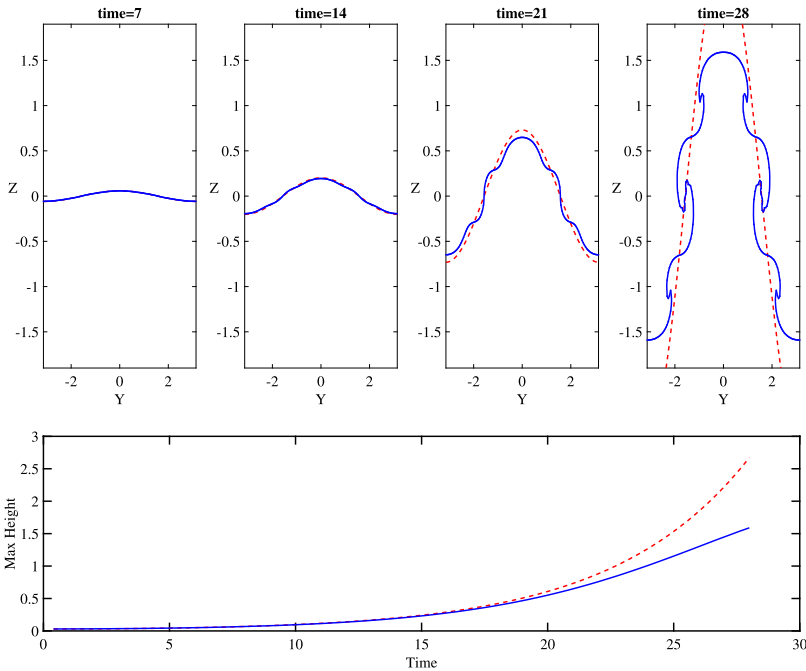
FIGURE 9. A comparison of the linearized inviscid model (dashed line) with the nonlinear viscous numerical model (solid line) at four dimensionless times, $t = 7, 14, 21, 28$. The top and bottom boundaries were set by $H_1 = H_2 = 2$. A slice of each at $x = 0$ has been shown in order to compare the linear and nonlinear results clearly. The interface in each model starts from rest at $t = 0$, with initial profile $z = 0.03 \cos x \cos y$. The two models are indistinguishable at $t = 7$ and very slightly different at $t = 14$. After that time, the two models diverge, with the linear model continuing to grow exponentially and the nonlinear model slowing and overturning. In the lower panel, we see the height of the interface directly above the origin ($x = y = 0$). The linear model (dashed) shows exponential growth, while the Boussinesq model (solid) has initial exponential growth, tempered by nonlinear effects at later times.

6.3. Comparison with linear approximation The linearized equation (3.9) presented in Section 3 predicts exponential growth of the interfacial perturbations. This should be very accurate for early times. In the nonlinear viscous model, however, at later times, viscosity will damp the flow, and the interface will roll over. As a necessary check on the accuracy of the numerical solution which we have provided, it is important to verify that the two approaches do in fact coincide for early times. In Figure 9, we present the linear solution overlaid on the numerical solution, for the case $H_1 = H_2 = 2, D = 1.05, \epsilon = 0.03$ and $\mu = \sigma = 10^{-4}$. The initial interface shape was set as $z = \epsilon \cos(x) \cos(y)$ for $-\pi < x < \pi, -\pi < y < \pi$. The nonlinear calculation was performed using 131 points and 52 modes in each direction. In order to compare the two clearly, we have taken a central slice at $x = 0$. The two models evolve very similarly at first, with the exponential growth predicted by the linear model also

dominating the nonlinear model. Viscosity and nonlinearity become more important factors at later times, damping the exponential growth and causing the interface to roll over, as expected. This agreement with the linearized theory gives confidence that the numerical model is accurately describing the evolution of the flow.

7. Conclusion

In this paper, we have calculated the evolution of the Rayleigh–Taylor instability in two and three dimensions. By bringing together several modern approaches to the problem, we have accurately modelled the time evolution of a fully 3D fluid system. The use of the spectral method combined with the bi-streamfunction approach has provided a very high degree of accuracy, and obviated the need to deal with either the pressure or the incompressibility condition, and allowed the use of exact derivatives and exponential convergence of integrals. This approach has resulted in a very large system of differential equations which can be integrated in parallel and which is, therefore, well suited to the capabilities of modern graphics processors. It may be seen that the linearized inviscid model gives excellent agreement with the numerical viscous model at early times, giving us confidence that both the numerical scheme and the linearization are accurate.

While this paper has focused on the Boussinesq approximation, the triple combination of vorticity equation, bi-streamfunction approach and spectral method is expected to be directly applicable to other suitable approximations of the Navier–Stokes equations, such as one in which the density ratio is very large (for example, in cosmic jets and bubbles). Also, we have shown that this method can be used for other interface shapes (the rising sphere in Figure 7) and for tracking the transport of properties other than density (the colliding blobs of fluid in Figure 8).

Acknowledgements

Appendix A. Differential equations for system of coefficients

In this paper, we have presented an approach to solving the viscous Rayleigh–Taylor problem using a spectral method. The set of equations is laid out here for completeness. These are three sets of m by n by p ordinary differential equations which are marched forward in time using the classical fourth-order explicit Runge–Kutta method. The integrals were performed using the trapezoidal method, which is exponentially accurate for periodic integrands [2, page 288]. The first two sets of these equations are derived by substituting the spectral representations (4.6) into the vorticity equation (4.4) and solving for dA/dt and dB/dt, while the third set is obtained

by substituting the series for $\tilde{\rho}$ (4.7) into the transport equation (4.3).

$$\frac{dA_{mnp}}{dt} = \frac{\alpha_m \alpha_n}{\alpha_p^2 \alpha_{mnp} V \gamma_{mn}} \int_{-\pi}^{\pi} \int_{-\pi}^{\pi} \int_{-h_1}^{h_2} [(\boldsymbol{\zeta} \cdot \boldsymbol{\nabla})u - (\boldsymbol{q} \cdot \boldsymbol{\nabla})\zeta^X] C_x S_y S_z \, dz \, dy \, dx$$

$$+ \frac{\alpha_n^2 + \alpha_p^2}{\alpha_p^2 \alpha_{mnp} V \gamma_{mn}} \int_{-\pi}^{\pi} \int_{-\pi}^{\pi} \int_{-h_1}^{h_2} [(\boldsymbol{\zeta} \cdot \boldsymbol{\nabla})v - (\boldsymbol{q} \cdot \boldsymbol{\nabla})\zeta^Y] S_x C_y S_z \, dz \, dy \, dx$$

$$- \frac{\alpha_m}{\alpha_{mnp}} C_{mnp} - \mu \alpha_{mnp} A_{mnp},$$

$$\frac{dB_{mnp}}{dt} = \frac{\alpha_m^2 + \alpha_p^2}{\alpha_p^2 \alpha_{mnp} V \gamma_{mn}} \int_{-\pi}^{\pi} \int_{-\pi}^{\pi} \int_{-h_1}^{h_2} [(\boldsymbol{\zeta} \cdot \boldsymbol{\nabla})u - (\boldsymbol{q} \cdot \boldsymbol{\nabla})\zeta^X] C_x S_y S_z \, dz \, dy \, dx \quad \text{(A.1)}$$

$$+ \frac{\alpha_m \alpha_n}{\alpha_p^2 \alpha_{mnp} V \gamma_{mn}} \int_{-\pi}^{\pi} \int_{-\pi}^{\pi} \int_{-h_1}^{h_2} [(\boldsymbol{\zeta} \cdot \boldsymbol{\nabla})v - (\boldsymbol{q} \cdot \boldsymbol{\nabla})\zeta^Y] S_x C_y S_z \, dz \, dy \, dx$$

$$- \frac{\alpha_n}{\alpha_{mnp}} C_{mnp} - \mu \alpha_{mnp} B_{mnp},$$

$$\frac{dC_{mnp}}{dt} = -\frac{1}{V \gamma_{mn}} \int_{-\pi}^{\pi} \int_{-\pi}^{\pi} \int_{-h_1}^{h_2} [(\boldsymbol{q} \cdot \boldsymbol{\nabla})\tilde{\rho}] C_x C_y S_z \, dz \, dy \, dx - \sigma \alpha_{mnp} C_{mnp}.$$

In these expressions, the quantities γ_{mn} are constants that arise in Fourier analysis for the (m, n)th mode at a fixed value of p. For m, n both nonzero, $\gamma_{mn} = 1$, but $\gamma_{01} = \gamma_{10} = 2$ and $\gamma_{00} = 4$. The volume constant, $V = 4\pi^2(H_1 + H_2)/8$, also results from Fourier decomposition and the orthogonality of the trigonometric modes. Additionally, the following abbreviations have been used:

$$S_x \equiv \sin(\alpha_m x),$$
$$C_x \equiv \cos(\alpha_m x),$$
$$S_y \equiv \sin(\alpha_n y),$$
$$C_y \equiv \cos(\alpha_n y),$$
$$S_z \equiv \sin(\alpha_p(z + H_1)),$$
$$C_z \equiv \cos(\alpha_p(z + H_1)).$$

We finally note that if half-mode basis functions are used (for example, $\alpha_m = m/2$ as discussed in the last paragraph of Section 4) some small modifications are required to the equations (A.1), since not all of the orthogonality conditions hold in that case.

References

[1] S. I. Abarzhi, "Review of theoretical modelling approaches of Rayleigh–Taylor instabilities and turbulent mixing", *Philos. Trans. R. Soc. Lond. Ser. A* **368** (2010) 1809–1828; doi:10.1098/rsta.2010.0020.

[2] K. E. Atkinson, *An introduction to numerical analysis*, 2nd edn (John Wiley, New York, 1978).

[3] G. K. Batchelor, *An introduction to fluid dynamics* (Cambridge University Press, Cambridge, 1967).

[4] J. P. Boyd, *Chebyshev and Fourier spectral methods* (Dover, New York, 2001).

[5]   B. J. Daly, "Numerical study of two fluid Rayleigh–Taylor instability", *Phys. Fluids* **10** (1967) 297–307; doi:10.1063/1.1762109.

[6]   D. E. Farrow and G. C. Hocking, "A numerical model for withdrawal from a two-layer fluid", *J. Fluid Mech.* **549** (2006) 141–157; doi:10.1017/S0022112005007561.

[7]   L. K. Forbes, "The Rayleigh–Taylor instability for inviscid and viscous fluids", *J. Engrg. Math.* **65** (2009) 273–290; doi:10.1007/s10665-009-9288-9.

[8]   L. K. Forbes and M. A. Brideson, "On modelling the transition to turbulence in pipe flow", *ANZIAM J.* **59** (2017) 1–34; doi:10.1017/S1446181117000256.

[9]   H. G. Lee and J. Kim, "Numerical simulation of the three-dimensional Rayleigh–Taylor instability", *Comput. Math. Appl.* **66** (2013) 1466–1474; doi:10.1016/j.camwa.2013.08.021.

[10] H. Liang, Q. X. Li, B. C. Shi and Z. H. Chai, "Lattice Boltzmann simulation of three-dimensional Rayleigh–Taylor instability", *Phys. Rev. E* **93** (2016) 033113; doi:10.1103/PhysRevE.93.033113.

[11] T. T. Lim and T. B. Nickels, "Instability and reconnection in the head-on collision of two vortex rings", *Nature* **357** (1992) 225–227; doi:10.1038/357225a0.

[12] PGI Community Edition, https://www.pgroup.com/products/community.htm (accessed 28 March 2019).

[13] Lord Rayleigh, "Investigation of the character of the equilibrium of an incompressible heavy fluid of variable density", *Proc. Lond. Math. Soc.* **14** (1883) 170–177; doi:10.1112/plms/s1-14.1.170.

[14] D. Sandlin, "Two vortex rings colliding in SLOW MOTION" (online video clip: *YouTube*, uploaded 20 June 2018, accessed 19 March 2019); https://www.youtube.com/watch?v=EVbdbVhzcM4.

[15] M. S. Shadloo, A. Zainali and M. Yildiz, "Simulation of single mode Rayleigh–Taylor instability by SPH method", *Comput. Mech.* **51** (2013) 699–715; doi:10.1007/s00466-012-0746-2.

[16] D. H. Sharp, "An overview of Rayleigh–Taylor instability", *Phys. D: Nonlinear Phenomena* **12** (1984) 3–18; doi:10.1016/0167-2789(84)90510-4.

[17] G. I. Taylor, "The instability of liquid surfaces when accelerated in a direction perpendicular to their planes. I", *Proc. R. Soc. Lond. Ser. A* **201** (1950) 192–196; doi:10.1098/rspa.1950.0052.

[18] H. Wilbraham, "On a certain periodic function", *Cambridge Dublin Math. J.* **3** (1848) 198–201; https://books.google.com.au/books?id=JrQ4AAAAMAAJ&pg=PA198&redir_esc=y#v=onepage &q&f=false.

[19] Y. Zhou, "Rayleigh–Taylor and Richtmyer–Meshkov instability induced flow, turbulence, and mixing. I", *Phys. Rep.* **720–722** (2017) 1–136; doi:10.1016/j.physrep.2017.07.005.

[20] Y. Zhou, "Rayleigh–Taylor and Richtmyer–Meshkov instability induced flow, turbulence, and mixing. II", *Phys. Rep.* **723–725** (2017) 1–160; doi:10.1016/j.physrep.2017.07.008.